



## Enhanced electrochemical oxidation of 5-hydroxymethylfurfural over tailored nickel nanoparticle assembly

Jiansong Wang<sup>a</sup>, Wenru Zhao<sup>a</sup>, Hui Yu<sup>a</sup>, Wei Wang<sup>a</sup>, Yipu Xu<sup>a</sup>, Liu-Liu Shen<sup>c,\*</sup>, Gui-Rong Zhang<sup>b,\*</sup>, Donghai Mei<sup>a,b,d,\*\*</sup>

<sup>a</sup> School of Materials Science and Engineering, Tiangong University, Tianjin 300387, PR China

<sup>b</sup> School of Chemical Engineering and Technology, Tiangong University, Tianjin 300387, PR China

<sup>c</sup> School of Chemistry, Tiangong University, Tianjin 300387, PR China

<sup>d</sup> School of Environmental Science and Engineering, Tiangong University, Tianjin 300387, PR China



### ARTICLE INFO

#### Keywords:

Nickel nanoparticles  
Particle aggregation  
5-hydroxymethylfurfural electro-oxidation  
phase transformation  
Operando spectroscopies

### ABSTRACT

Nickel-based materials are promising electrocatalysts for anodic oxidation of 5-hydroxymethylfurfural (HMF) to value-added 2, 5-furandicarboxylic acid (FDCA). However, their catalytic efficiency is impeded by the sluggish phase transformation of Ni(II) hydroxide to the active Ni(III) oxyhydroxide. Herein, we demonstrate for the first time that the phase transformation kinetics and the HMF oxidation activity of nickel nanoparticles can be modulated by creating self-assemblies with different particle aggregation structures: ordered nanoarrays, disordered nanoarrays, and random aggregates. Notably, the nanoparticle assembly featuring an ordered nanoarray structure exhibits the highest activity, achieving 99.8 % HMF conversion and 99.2 % FDCA yield at 1.36 V. *In situ* Raman spectroscopy and electrochemical analysis reveal that the ordered nanoarray effectively accelerates the transformation kinetics, attributed to the reduced dehydrogenation barrier of Ni(II) hydroxide as confirmed by density functional theory calculations. This work contributes new insights into the structure-performance relationship of Ni-based catalysts, offering valuable guidance for designing high-performing electrocatalysts.

### 1. Introduction

The valorization of biomass has the potential to supplement or partially replace fossil resources for fuel/chemical synthesis [1–3]. 5-Hydroxymethylfurfural (HMF) is an important bio-based platform molecule acting as a pivotal linkage between biomass and numerous high-value chemicals [4,5]. Notably, 2, 5-furandicarboxylic acid (FDCA) stands out as a key derivative of HMF, serving as a precursor for diverse chemicals such as polyester, polyimide and polyurethane. The electrochemical HMF oxidation reaction (HMFOR) is a promising approach to producing FDCA, offering the advantage of ambient temperature operation and the elimination of the requirements for O<sub>2</sub> or other hazardous oxidants typically involved in the conventional heterogeneous catalytic aerobic oxidation processes [6,7]. Moreover, this approach could improve energy efficiency when paired with reactions such as electrochemical CO<sub>2</sub> reduction and hydrogen evolution [8,9]. However, the technoeconomic feasibility of HMFOR is impeded by the performance of

electrocatalysts, which face two primary challenges: the competing oxygen evolution reaction (OER) that diminishes the Faradaic efficiency (FE) of HMFOR [10,11], and the high reaction overpotential that escalates the electric energy input [12,13].

Recently, Ni-based materials have emerged as superior electrocatalysts for the HMFOR [14–16]. Extensive research work has been dedicated to enhancing their catalytic efficiency by engineering their size, morphology and surface composition [17–19]. A primary objective of these studies is to facilitate the phase transformation of Ni(II) hydroxide to Ni(III) oxyhydroxide [20–23], as the resultant Ni(III) sites are postulated to be the active centers that enable the adsorption and activation of HMF molecules [14,16,24], as well as the subsequent dehydrogenation processes [25]. The kinetics of this phase transformation thus plays an essential role in determining the overall catalytic efficiency of Ni-based catalysts. Lowering the activation energy barrier and triggering the phase transformation at low overpotential are critical for enhancing their electrocatalytic performance.

\* Corresponding authors.

\*\* Corresponding author at: School of Materials Science and Engineering, Tiangong University, Tianjin 300387, PR China.

E-mail addresses: [shenli.liu@tiangong.edu.cn](mailto:shenli.liu@tiangong.edu.cn) (L.-L. Shen), [grzhang@tiangong.edu.cn](mailto:grzhang@tiangong.edu.cn) (G.-R. Zhang), [dhmei@tiangong.edu.cn](mailto:dhmei@tiangong.edu.cn) (D. Mei).

Some trial-and-error design strategies have been employed to hasten the phase transformation, such as heterostructure coupling, defect engineering, and heteroatom doping. For instance, Wang et al. [26] reported that the Pt modified  $\text{Ni(OH)}_2$  serves as an active catalyst for the HMFOR. The introduction of Pt lowered the dehydrogenation energy barrier of  $\text{Ni(OH)}_2$ , accelerating the formation of active  $\text{Ni(III)}$  intermediate, resulting in an 8.2-fold enhancement in current density compared to the pristine  $\text{Ni(OH)}_2$ . Likewise, Bedford and co-workers [27] demonstrated that Ce-doping could incorporate oxygen vacancies ( $\text{V}_\text{O}$ ) into Co-Ni layered double hydroxides (LDHs). The presence of Ce and  $\text{V}_\text{O}$  promoted the transformation of LDH into active oxyhydroxide, enhancing electrocatalytic activity compared to the unmodified Co-Ni LDH. Gao et al. [28] demonstrated that the electron deficient B acted as an “electron sink”, facilitating electrons flow from the  $\text{Ni}^{2+}$  site and leading to the formation of  $\text{Ni}^{3+\delta}$  active species at a lower potential. These previous inspiring works clearly demonstrate the significance of the phase transformation in forming active electrocatalysts toward the HMFOR. However, much of this research has concentrated on the inherent electronic and geometric structures of the catalysts, with scant attention given to the physical aggregation structure of nanoparticles (NPs). This aggregation structure is vital for defining the interfacial structure between the solid catalyst and liquid electrolyte, presenting a significant opportunity to further enhance HMFOR efficiency.

Herein, as a proof-of-concept, we tailored the aggregation structures of Ni NPs by constructing distinct self-assemblies, namely ordered nanoarrays, disordered nanoarrays and random aggregates, using a facile potentiometric electrodeposition method. Our findings reveal that, despite the usage of identical particles in constructing these self-assemblies, their unique aggregation structure significantly influences the HMFOR activities. Specifically, the Ni NPs assembly with an ordered nanoarray structure exhibits outstanding HMFOR activity, achieving an impressive 99.8 % HMF conversion, 99.2 % FDCA selectivity, and 99.1 % Faradaic efficiency (FE) at an exceptionally low potential of 1.36 V, accompanied by a robust stability with no activity loss over 10 electrolysis cycles. Through comprehensive *in situ* Raman, X-ray photoelectron spectroscopy (XPS) and electrochemical voltammetry/impedance analyses, we unambiguously confirmed that the ordered nanoarray of Ni NPs had the fastest phase transformation kinetics. The superior performance of ordered nanoarray of Ni NPs would benefit from the efficient contact between the catalyst surface and the electrolyte, which can reduce the dehydrogenation barrier of  $\text{Ni(II)}$  hydroxide as implied by the density functional theory (DFT) calculations, thereby promoting the formation of active  $\text{Ni(III)}$  oxyhydroxide. This work would significantly improve our fundamental understanding about the influence of the particle aggregation structure on catalytic properties, and at same time provides a refreshing perspective for developing high performance electrocatalysts through rational tailoring of particle aggregation structure.

## 2. Experimental section

### 2.1. Chemicals

Nickel sulfate hexahydrate ( $\text{NiSO}_4 \cdot 6 \text{ H}_2\text{O}$ , 99.9 %), ammonium formate ( $\text{HCOO}(\text{NH}_4)$ , ≥ 99 %) and potassium hydroxide (KOH, 95 %) were purchased from Macklin Biochemical Co., Ltd. 5-Hydroxymethyl-furfural (HMF, 99 %), 2, 5-Diformylfuran (DFF, ≥ 98 %), 5-Hydroxymethyl-2-furancarboxylic acid (HMFCA, 98 %), 5-Formyl-2-furancarboxylic acid (FFCA, ≥ 98 %) and 2, 5-Furandicarboxylic acid (FDCA, 98 %) were purchased from Aladdin Chemistry Co., Ltd. Methyl alcohol (for HPLC, ≥ 99.9 %) were obtained Sinopharm Chemical Reagent Co., Ltd. All chemicals were used as received without further purification. The deionized water was purified from HHitech water purification system and used in all experiments.

### 2.2. Synthesis of carbon paper supported Ni NPs

The carbon paper (CP) was first cut into rectangular pieces with dimensions of 1 cm × 2 cm. Prior to use, the CP was successively ultrasonicated in acetone, ethanol, and deionized water for 10 min to remove residual impurities and dried under vacuum at 60 °C overnight. The deposition area was accurately controlled to 1 cm<sup>2</sup> by paraffin film. Electrodeposition was performed at 25 °C in a 50 mL electrolytic bath. In a typical electroplating experimental setup, a standard three-electrode system was employed, a piece of CP, a graphite plate and a Hg/HgO (1 M KOH) served as the working, counter and reference electrode, respectively. These electrodes were housed within an undivided cell and regulated by a CHI 760E electrochemical workstation under ambient environmental conditions. The electrolyte was 30 mL of 1 M  $\text{NiSO}_4 \cdot 6 \text{ H}_2\text{O}$  aqueous solution. Electrodeposition of Ni on CP were performed at current density of  $-1.5 \text{ mA} \cdot \text{cm}^{-2}$ ,  $-3.0 \text{ mA} \cdot \text{cm}^{-2}$  and  $-4.5 \text{ mA} \cdot \text{cm}^{-2}$ , were denoted as Ni/CP-1.5, Ni/CP-3.0 and Ni/CP-4.5, respectively. The deposition amount of Ni was accurately controlled at 1 mg·cm<sup>-2</sup> by controlling the deposition time. The prepared samples were rinsed with deionized water and dried under  $\text{N}_2$  purge.

### 2.3. Characterization

Thermogravimetric analysis (TGA) data were obtained by using a NETZSCH TG 209 F3 Tarsus analyzer with a heating rate of 10 °C·min<sup>-1</sup> under air atmosphere. The scanning electron microscope (SEM) images were obtained by a SEM (HITACHI FE-SEM-4800) with a 1 kV accelerating voltage. X-ray diffraction (XRD) patterns of the samples were obtained with a BRUKER D8 ADVANCE X-ray diffractometer using the  $\text{Cu K}\alpha$  radiation source with a wavelength of 1.54 Å. The diffraction data were taken in the 2θ range from 5 to 80° with a step size of 0.01°. Transmission electron microscopy (TEM) analyses were performed on an H7650 microscope (Hitachi) with an acceleration voltage of 100 kV. High-resolution transmission electron microscopy (HR-TEM) images were captured using a JEM-F200 microscope (JEOL) equipped with an X-ray detector operated at an acceleration voltage of 200 kV. X-ray photoelectron spectroscopy (XPS) spectra were recorded on a Thermo Fisher NEXSA XPS spectrometer, and the binding energies were calibrated against the C 1 s signal of adventitious carbon at 284.8 eV.

### 2.4. Electrochemical measurements

Electrochemical tests were carried out on a CHI 760E instrument electrochemical workstation, using a typical three-electrode configuration. The as-prepared Ni/CP clamped with platinum electrode clamps was directly used as the working electrode, Pt foil as the counter electrode, and Hg/HgO (1 M KOH) as the reference electrode. LSV was measured at a scan rate of 10 mV·s<sup>-1</sup> in an undivided cell, and constant potential electrolysis experiments were performed in an H-type electrolytic cell separated by Nafion 117 membranes. The anolyte contained 10 mL of  $\text{N}_2$ -saturated freshly prepared 0.1 M KOH solution (pH=13) and 5 mM HMF, and the catholyte contained 10 mL of 0.1 M KOH solution. All electrochemical reactions were carried out at room temperature (25 °C), and the electrolyte was stirred at 1200 rpm with a magnetic stirrer (Model: IKA MYPLATE S025). All of the reported potentials were converted to the reversible hydrogen electrode (RHE) scale using  $E_{\text{RHE}} = E_{\text{Hg/HgO}} + 0.0591 \times \text{pH} + 0.095 \text{ V}$ . Unless otherwise specified, all potentials are referenced to RHE. *In situ* electrochemical impedance spectroscopy (EIS) measurements were conducted with a three-electrode system. The frequency ranged from 10000 to 0.01 Hz with an amplitude of 5 mV. The ECSA can be calculated from the double-layer capacitance ( $C_{\text{dl}}$ ) using the following equation:  $\text{ECSA} = S^*C_{\text{dl}}/C_s$ . Wherein, the  $S$  represents the geometric surface area of the working electrode, and  $C_s$  is specific electrochemical double-layer capacitance (0.04 mF·cm<sup>-2</sup> in alkaline media).

## 2.5. In situ raman spectroscopy

In situ Raman spectra were carried out on a laser confocal Raman spectroscopy (HORIBA Xplora Plus, France). All the electrochemical tests were carried out using the three-electrode configuration connected to an electrochemical workstation (CHI 760E). The electrolytic cell for *in situ* Raman Spectrum comprises a Peek shell, quartz glass plate, Pt wire, and Ag/AgCl electrodes. A silicon wafer (520.7 cm<sup>-1</sup>) was used to routinely calibrate the spectral shifts. The 785 nm laser with a power of 50 mW was selected and the spot size of the laser beam was estimated to be 1–2 μm. The Raman spectra of Ni/CP electrode were recorded for 20 s with 2 sweeps from 50 to 1100 cm<sup>-1</sup> under different potentials of 1.00–1.60 V and different reaction times in HMF-containing KOH electrolyte. The other conditions were the same as those used for electrochemical measurements.

## 2.6. Product analysis for HMFOR

The HMF and oxidation products were analyzed by high-performance liquid chromatography (HPLC, Agilent 1260 Infinit II) using a 4.6 mm × 150 mm Poroshell 120 4.0 μm C-18 column and the detection wavelength set at 265 nm. The column oven temperature was maintained at 40 °C. The mobile phase A was methanol and phase B was 5 mM ammonium formate aqueous solution, the ratio of A: B was 2:8, flow rate is 0.6 mL·min<sup>-1</sup>. 10 μL of electrolyte was removed during potentiostatic electrolysis and diluted to 1 mL with ultrapure water and analyzing it by HPLC. The quantification of HMF and oxidation products was calculated based on the calibration curves. The HMF conversion, the product yield, and the FE value of FDCA were calculated using the following equations, where *F* is Faraday's constant (96,485 C·mol<sup>-1</sup>).

$$\text{HMF conversion (\%)} = \frac{\text{mol of HMF consumed}}{\text{mol of initial HMF}} \times 100\%$$

$$\text{FDCA yield (\%)} = \frac{\text{mol of FDCA formed}}{\text{mol of initial HMF}} \times 100\%$$

$$\text{Faradaic efficiency (\%)} = \frac{\text{mol of FDCA formed}}{\text{total charge passed}/(6 \times F)} \times 100\%$$

## 2.7. Computational details

All periodic DFT calculations were performed with mixed Gaussian and plane wave basis sets implemented in the CP2K code [29]. The core electron was represented by norm-conserving Goedecker-Teter-Hutter pseudopotentials [30–32], and the valence electron wavefunctions were expanded in a triple-zeta basis set with polarization functions [33], along with an auxiliary plane wave basis set with an energy cutoff of 500 Ry. The generalized gradient approximation exchange-correlation functional of Perdew, Burke, and Enzerhof (PBE) was used [34]. For a better description of Ni 3d electrons, the Hubbard effective terms  $U_{\text{eff}} = 5.96$  eV were added to the PBE functional [35]. Test calculations showed that the total energy change of the system was negligible (< 0.01 eV) when the maximum force convergence criteria of 0.001 Hartree/Bohr was used. Each reaction intermediate structure was optimized with the Broyden-Fletcher-Goldfarb-Shanno (BFGS) algorithm with the SCF convergence criteria of  $1.0 \times 10^{-8}$  a.u. To account for the long-range van der Waals (vdW) interactions, the DFT-D3 scheme with an empirical damped potential term was added to the electronic energy [36]. The climbing image elastic band (CI-NEB) method [37,38] was used to determine the transition states of all elementary reaction steps in the bond scissions and recombination of O-H bond. The transition state was located with five intermediate images along the reaction pathway between the initial and final states. The Ni(OH)<sub>2</sub> was modelled with two layers (4 × 4) supercell. A vacuum of 10 Å in the z direction of the simulation box was inserted for each surface model.

*Ab initio* molecular dynamics (AIMD) simulations were performed to

calculate the diffusion coefficients of an OH<sup>-</sup> ion in the monolayer and bulk Ni(OH)<sub>2</sub> systems at 303.15 K. The temperature of AIMD simulations was controlled using a Nosé thermostat. Production runs were 5 ps. A time step of 0.5 fs was used in the AIMD simulations. The diffusion coefficients were computed from the mean square displacement (MSD) using the Einstein equation [39]:

$$D = \frac{1}{6} \lim_{t \rightarrow \infty} \frac{d}{dt} \langle (r(t) - r(0))^2 \rangle$$

where  $r(t)$  is the position of the OH<sup>-</sup> at time  $t$ . The slope of MSD versus time in the normal diffusion region was estimated as the diffusion coefficient.

## 3. Results

### 3.1. Synthesis and characterizations

The carbon paper supported Ni NP assemblies were synthesized by a facile potentiometric electrodeposition method, with their aggregation structures tailored by varying the electrodeposition current densities, as illustrated in Fig. 1a. The scanning electron microscope (SEM) images show that the electrodeposition current density significantly affect the aggregation structure of Ni NPs (Fig. 1b-d, Fig. S1). Specifically, the Ni/CP-1.5 sample consists of Ni NPs assembled into ordered nanoarrays with a lateral size of 200–300 nm (Fig. 1b). Increasing the electrodeposition current density can endow the Ni NP assemblies with pronounced disordered structures. The Ni/CP-3.0 retains the nanoarray structure but with a disordered packing of Ni NPs (Fig. 1c), while the Ni/CP-4.5 sample features random aggregates of Ni NPs without any ordered structure (Fig. 1d).

This unique correlation between particle aggregation structure and current density is not surprising as the electrodeposition current density is pivotal in determining both the nucleation and growth rate of Ni NPs on the CP support [40–42]. Under high electrodeposition current density, a large number of Ni NPs form in a short time, leaving no enough time and space for them to assemble into ordered structures before forming random aggregates [43]. For a fair comparison of their catalytic performance, we controlled the deposition amounts of Ni on CP for all three samples at 1 mg·cm<sup>-2</sup> by adjusting the electrodeposition time (Fig. S2). The thermal gravimetric analyses (TGA) also confirmed that despite their dramatically different aggregation structures, the Ni masses on CP for all these three samples are in a comparable range (Fig. S3 and Table S1).

X-ray diffraction (XRD) analysis was employed to investigate the crystalline structure of the as-synthesized Ni/CP samples. As shown in Fig. 2a, the diffraction peaks at angles of 44.5°, 51.8°, and 76.4° correspond to the (111), (200), (220) planes of metallic Ni<sup>0</sup> (JCPDS card No. 04–0850), signifying that metallic Ni<sup>0</sup> is the dominant component in all freshly prepared samples. Transmission electron microscopy (TEM) characterizations confirm that Ni NP assemblies essentially consist of identical Ni NPs with an average diameter of ~ 26 nm (Fig. 2b and Fig. S4a-b), regardless of their initial aggregation structures. The high resolution TEM (HR-TEM) in conjunction with fast Fourier-transform (FFT) analyses of Ni/CP-1.5 disclosed the face-centered cubic (FCC) crystalline structure of the Ni NPs. The lattice spacings of 0.124, 0.176, and 0.203 nm correspond to the (220), (200), and (111) planes in metallic Ni<sup>0</sup>, respectively (insets in Fig. 2b and Fig. S4a-b) [44,45]. This finding aligns with the observed XRD patterns. The comparable HR-TEM and FFT patterns of all three samples again confirm their identical crystalline structure regardless of the particle aggregation structure, which offers a solid basis for assessing the influence of the particle aggregation structure on their electrocatalytic properties.

Fig. 2c and Fig. S5 presents the X-ray photoelectron spectroscopy (XPS) spectra of Ni/CP-1.5 before and after contact with the alkaline electrolyte. The Ni 2p signals confirm the presence of both Ni<sup>0</sup> and Ni<sup>2+</sup>

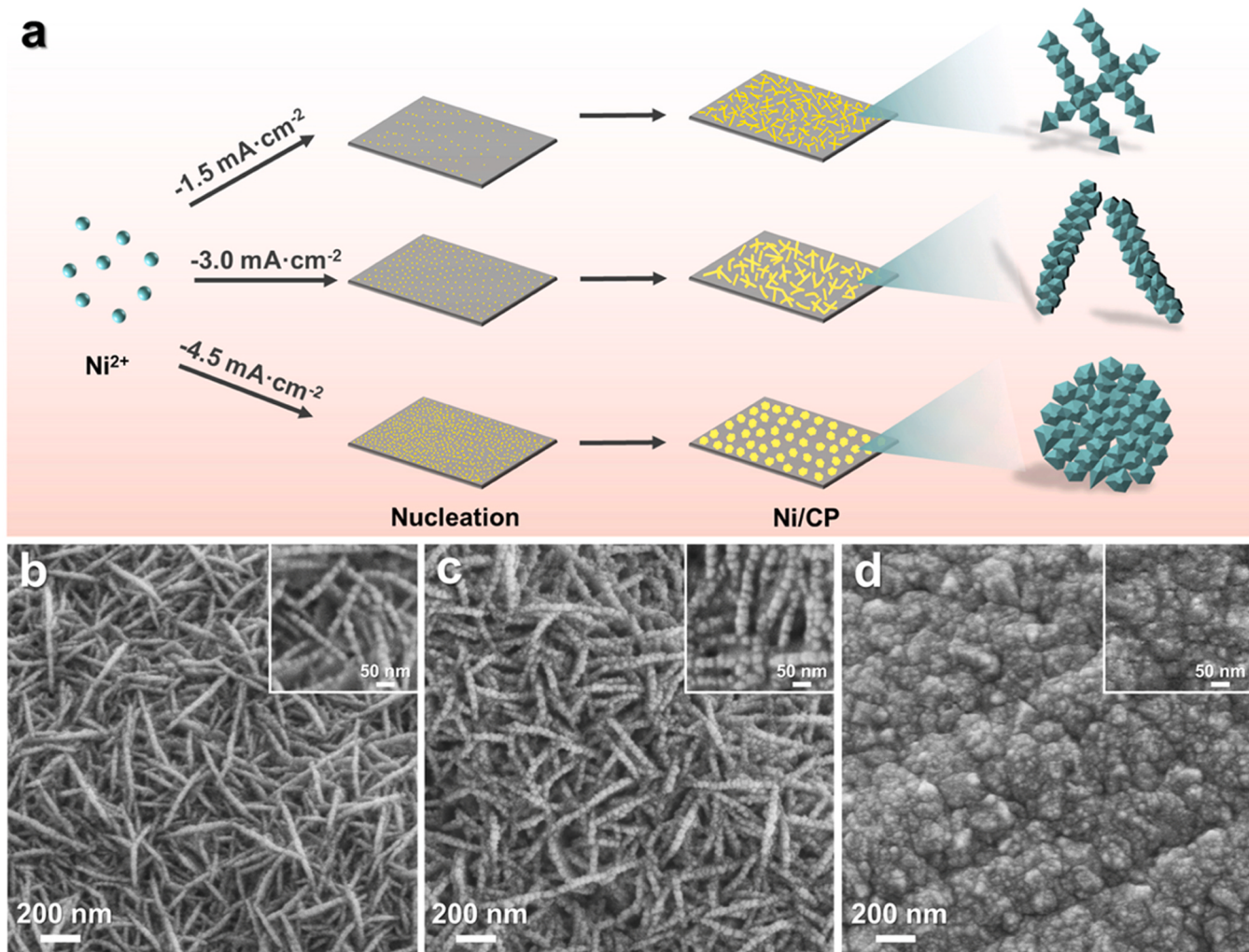


Fig. 1. (a) Schematic illustration of the preparation procedure for Ni/CP. SEM images of different morphology of Ni/CP electrodes: (b) Ni/CP-1.5, (c) Ni/CP-3.0 and (d) Ni/CP-4.5.

on the surface of the as-synthesized Ni/CP samples. This dual presence is not surprising given the spontaneous oxidation of metallic Ni to Ni<sup>2+</sup> upon exposure to air [46,47]. Interestingly, upon immersion in the alkaline electrolyte, the surface Ni species exists exclusively as Ni<sup>2+</sup>, due to the surface hydroxylation of metallic Ni [21,28]. To further investigate the oxidation state transitions of Ni, Raman spectra were recorded (Fig. 2d and Fig. S6). Two distinct Raman signals at 449 and 527 cm<sup>-1</sup> become evident after exposing the samples to the alkaline electrolyte; these signals correspond to the vibrations of Ni<sup>2+</sup>-OH and Ni<sup>2+</sup>-O bonds of Ni(OH)<sub>2</sub> [22,48–51], which further corroborates the rapid hydrolyzation of surface Ni<sup>0</sup> to form Ni(OH)<sub>2</sub> in alkaline electrolyte. These results indicate that the “pre-catalyst” changes from Ni<sup>0</sup> to Ni(OH)<sub>2</sub> state in alkaline electrolyte prior to the commencement of the electrochemical oxidation reaction.

### 3.2. Electrocatalytic HMFOR performance

The electrocatalytic HMFOR performance of the as-synthesized materials was first evaluated in 0.1 M KOH with 5 mM HMF electrolyte using a three-electrode configuration. Fig. 3a illustrates the linear sweep voltammetry (LSV) curves of Ni/CP-1.5 in 0.1 M KOH with and without 5 mM HMF. All polarization curves were presented without iR compensation. In the absence of HMF, a distinct peak around 1.45 V corresponds to the oxidation of Ni<sup>2+</sup> to Ni<sup>3+</sup> [52–54]. The current density increases with in presence of HMF, indicating that the

electrochemical HMFOR occurs simultaneously with the oxidation of the electrode from Ni<sup>2+</sup> to Ni<sup>3+</sup>. This phenomenon is also observed in Ni/CP-3.0 and Ni/CP-4.5 (Fig. S7), indicating that all three catalysts despite possessing different particle aggregation structures, show activity for electrochemical HMFOR.

The HMFOR performance of different electrodes are compared in Fig. 3b. It is evident that the Ni/CP-1.5 with ordered nanoarray morphology owns the lowest onset potential (defined here as the potential at 2 mA·cm<sup>-2</sup>) of 1.33 V and the most significant current density enhancement due to the HMF oxidation compared with Ni/CP-3.0 (1.35 V) and Ni/CP-4.5 (1.39 V) electrodes. Meanwhile, the corresponding Tafel slopes were calculated to assess the kinetics of the electrochemical HMFOR. As depicted in Fig. 3c, Ni/CP-1.5 shows the lowest Tafel slope of 80.6 mV·dec<sup>-1</sup>, much lower than those of Ni/CP-3.0 (94.2 mV·dec<sup>-1</sup>) and Ni/CP-4.5 (106.5 mV·dec<sup>-1</sup>), indicating the fastest electron transfer kinetics at the interface between the HMF molecule and Ni/CP-1.5 electrocatalyst. The same conclusion can also be reached by the electrochemical impedance spectroscopy (EIS) analyses. The Nyquist plots were fitted using a Randles-type equivalent circuit model (Fig. S8), with the fitting parameters presented in Table S2. Fig. 3d shows the Nyquist plots of Ni/CP-1.5, -3.0 and -4.5 at 1.36 V in 0.1 M KOH electrolyte with 5 mM HMF, from which it can be seen that Ni/CP-1.5 features a well-defined semicircle with the smallest diameter, reflecting a reduced charge transfer resistance relative to the other counterparts.

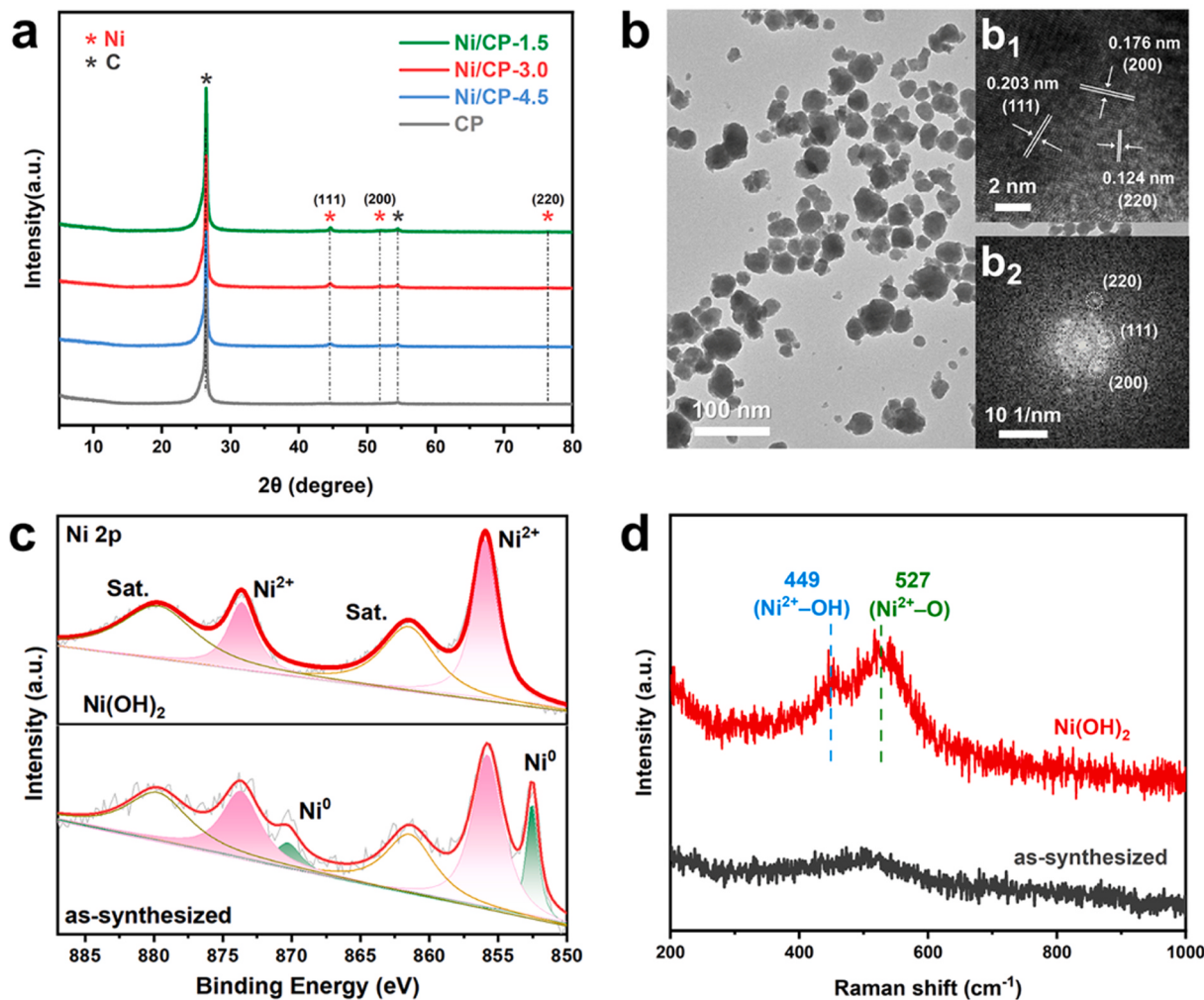


**Fig. 2.** (a) XRD patterns of Ni/CP-1.5, Ni/CP-3.0 and Ni/CP-4.5. (b) TEM image of Ni/CP-1.5; Fig. insets are the HR-TEM (b<sub>1</sub>) and SAED (b<sub>2</sub>) patterns of Ni/CP-1.5. The Ni 2p XPS spectra (c) and the Raman spectra (d) of as-synthesized and surface hydroxylated Ni/CP-1.5.

It is also found that the particle aggregation structure can affect the electrochemically active surface area (ECSA) of Ni NPs which is quantified by the double layer capacitance (Fig. 3e and Fig. S9). The Ni/CP-1.5 exhibits a specific capacitance as high as  $2.7 \text{ mF cm}^{-2}$ , almost twice that of Ni/CP-4.0 with random aggregation structure. To discern whether the superior HMFOR activity of Ni/CP-1.5 originates solely from its higher ECSA, herein we also quantify their intrinsic activity in terms of both the ECSA-normalized HMFOR current density and the turnover frequency (TOF, as detailed in the Fig. S10) based on exposed Ni sites. As compiles in Fig. 3f, the Ni/CP-1.5 can still exhibit the highest intrinsic activity among all three samples, indicating that the particle aggregation structure can not only influence the exposed surface area of the active phase, but also impose profound impact on the reaction kinetics of the catalysts. This will be elaborated further in the following section. These results provide the first piece of evidence that the intrinsic activity of Ni NPs toward the HMFOR is highly sensitive to their particle aggregation structure.

Chronoamperometric electrolysis of HMF to FDCA was carried out at various potentials in a 10 mL solution of 0.1 M KOH with 5 mM HMF, using an H-cell separated by a Nafion membrane (Fig. 4a). As shown in Fig. S11, the chronoamperometric curves recorded during the HMFOR demonstrate a continuous decrease in current density over time, indicative of the ongoing consumption of HMF. The HMF conversion, product yield, and FE for FDCA production after passing the stoichiometric amount of change to convert HMF to FDCA for each sample were

summarized in Table S3.

There are two possible pathways for HMF oxidation to FDCA due to the coexistence of hydroxyl and aldehyde groups on HMF (Fig. 4b) [5, 55,56]. In Path 1, aldehyde groups are preferentially oxidized to carboxylic groups, leading to the formation of the intermediate 5-hydroxy-methyl-2-furancarboxylic acid (HMFCA). Conversely, Path 2 involves oxidation of the hydroxyl group into the aldehyde group, yielding dialdehyde 2, 5-diformylfuran (DFF). Both HMFCA and DFF are subsequently oxidized to 5-formyl-2-furancarboxylic acid (FFCA) and ultimately to FDCA. The electrocatalytic HMFOR performance over Ni/CP-1.5 was first evaluated at 1.36 V. High-performance liquid chromatography (HPLC) was used to monitor the concentrations of HMF and its oxidation products quantitatively by periodically collecting the resultant electrolytes (Fig. 4c). Fig. S12 shows the peak position of the standard substance as determined by liquid chromatography and the standard curve for HMF and oxidation products. As shown in Fig. 4d, as the charge increases, the concentrations of HMF and its oxidation products declines while the prevalence of FDCA boosts, suggesting successful conversion of HMF to FDCA. It is noteworthy that HMFCA and FFCA were detected during electrolysis, while DFF was absent. Similar observations apply to Ni/CP-3.0 and Ni/CP-4.5 catalysts (Fig. S13), indicating that the electrocatalytic HMFOR on Ni/CP electrodes proceeds via path 1.

Intriguingly, Ni/CP-1.5 demonstrates extraordinary electrocatalytic HMFOR performance at 1.36 V, featuring HMF conversion as high as

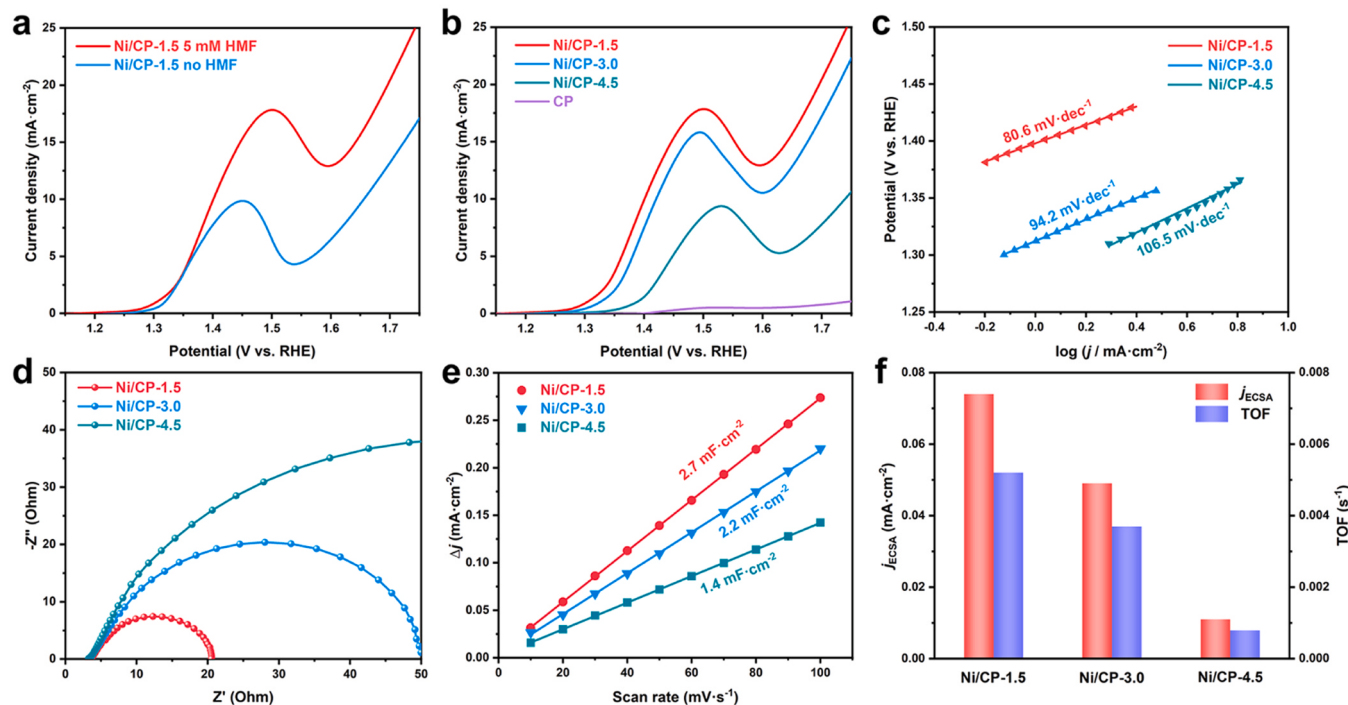


**Fig. 3.** (a) LSV curves of Ni/CP-1.5 in 0.1 M KOH with and without 5 mM HMF. (b) LSV curves of Ni/CP-1.5, Ni/CP-3.0, Ni/CP-4.5 and CP in 0.1 M KOH with 5 mM HMF. (c) The corresponding Tafel plots of Ni/CP-1.5, Ni/CP-3.0 and Ni/CP-4.5. (d) Nyquist plots of Ni/CP-1.5, Ni/CP-3.0 and Ni/CP-4.5 at 1.36 V. (e) The double-layer capacitances of Ni/CP-1.5, Ni/CP-3.0, and Ni/CP-4.5. (f) The current density after ESCA normalization and TOF of Ni/CP-1.5, Ni/CP-3.0 and Ni/CP-4.5 at 1.36 V.

99.8 %, and FDCA yield and FE up to 99.2 % and 99.1 %, respectively. In contrast, notable amount of HMF can still be detected on Ni/CP-3.0 and Ni/CP-4.5 after electrolysis, indicating their inefficiency in converting HMF at such a low potential (Fig. 4e and Table S3). When the electro-oxidation potential of HMF is increased to 1.40 V (Fig. S14 and Table S3), Ni/CP-1.5 continues to exhibit the highest FDCA yield (99.4 %) and FE (99.3 %), still well beyond those of Ni/CP-3.0 (yield: 94.7 %; FE: 96.4 %). To be noted, the Ni/CP-4.5 with random aggregation morphology is still incapable of fully converting HMF at 1.40 V. When the electrode potential is increased to 1.45 V, all three catalysts attains satisfactory levels of performance (Fig. S15 and Table S3). These results affirm that the substantial correlation between the electro-catalytic HMFOR performance and the particle aggregation structure of the catalysts. Remarkably, Ni/CP-1.5 with ordered nanoarray morphology showcases not only outstanding FDCA yield and FE among three catalysts, but also demonstrates the most favorable FDCA production rate at different potentials (Fig. 4f). In addition, the proposed Ni/CP-1.5 catalyst also exhibits remarkable durability. No obvious decay in HMF conversion, FDCA yield, and FE is observed after 10 consecutive electrolysis cycles (Fig. 4g). Overall, the above results highlight the extraordinary catalytic performance of Ni/CP-1.5 for electrocatalytic HMFOR. The electrocatalytic HMFOR activity of Ni/CP-1.5 surpasses most of the reported Ni-based catalysts (Fig. 4h and Table S4), making Ni/CP-1.5 one of the most efficient catalysts for electrocatalytic HMFOR.

To explore the potential application of the proposed Ni NP self-assemblies in the oxidation of diverse organic molecules, herein, we also made attempt to investigate the electrochemical oxidation performance of Ni/CP catalysts across various biomass substrates. Fig. S16 illustrates the LSV curves for the electrochemical oxidation of methanol, ethanol, isopropanol, benzyl alcohol, acetaldehyde, and benzaldehyde on three Ni/CP catalysts. Ni/CP electrodes can still exhibit fairly high activity, suggesting the broad applicability of the proposed Ni-based electrocatalysts toward the oxidation of alcohols or aldehydes. Notably, Ni/CP-1.5 consistently exhibits superior activity in these

reactions, further underscoring the pivotal influence of particle aggregation structure on electrooxidation processes and affirming that an ordered nanoarray structure is indeed conducive to enhanced electrocatalytic performance.

Moreover, for practical application, the electrolysis is usually conducted at relatively high current density. As shown in Fig. S17, the current density of Ni/CP-1.5 for electrochemical HMFOR significantly increases when the electrolyte is replaced with 1 M KOH with 50 mM HMF. Notably, even at a low potential of 1.36 V, the current density remains above  $20 \text{ mA}\cdot\text{cm}^{-2}$ , with FDCA yield and FE reaching 98.6 % and 98.1 %, respectively. These results suggest that Ni/CP-1.5 holds promise for practical applications. Nevertheless, further increasing the HMF concentration might accelerate the non-Faradaic processes, leading to the formation of undesired humin byproducts through decomposition and self-polymerization. Consequently, further extensive studies are still required to efficiently suppress the non-Faradaic processes in concentrated substrates.

#### 4. Discussion

The above results provide compelling evidence that the particle aggregation structure imposes a profound effect on the HMFOR activity of Ni-based electrocatalysts. However, the mechanism for how an ordered structure can more effectively boost the reaction rate at a relatively low overpotential remains elusive. As identified from the previous XPS analyses, Ni species in all three samples exist exclusively as  $\text{Ni}(\text{OH})_2$  in alkaline electrolyte. It is also well documented that the formed  $\text{Ni}(\text{OH})_2$  actually serves as a so-called “pre-catalyst” for the subsequent electrochemical oxidation processes, and when subjected to a sufficiently positive potential,  $\text{Ni}(\text{OH})_2$  can transform into the catalytically active Ni (III) oxyhydroxide phase [55,57]. Therefore, promoting this phase transformation kinetics is believed to be key to enhancing the HMFOR activity and has been a long endeavor for the research in this field.

Herein, we first probe the oxidation state of the Ni species in Ni/CP samples post-HMF electrolysis at varying electrode potentials using XPS

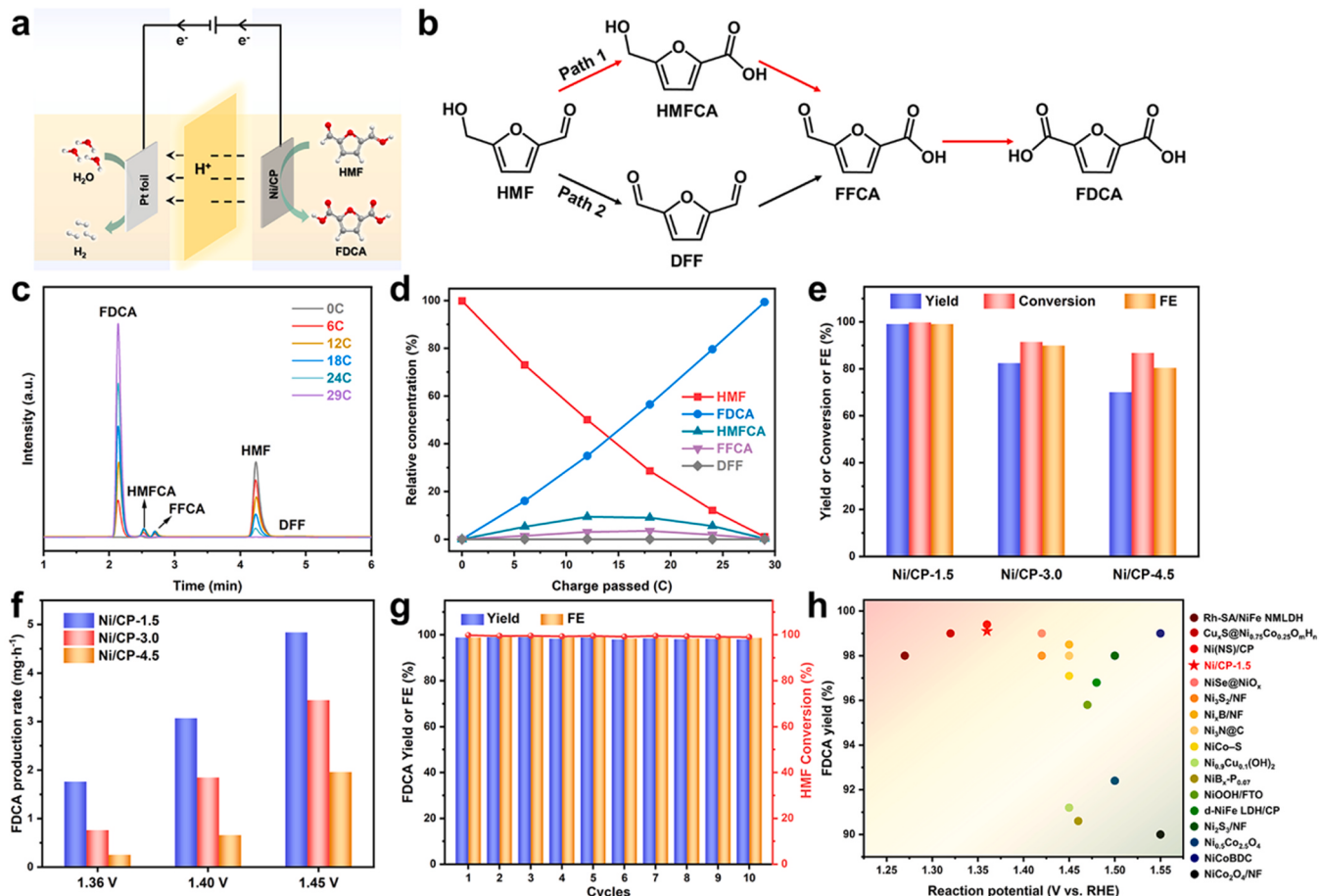


**Fig. 4.** (a) Electrochemical system for the oxidation of HMF. (b) Two possible pathways for the oxidation of HMF to FDCA. (c) High-performance liquid chromatography chromatogram of Ni/CP-1.5 obtained at various electrolysis charges at 1.36 V. (d) The corresponding concentration changes of HMF and its oxidation products during electrocatalytic HMFOR. (e) Conversion of HMF, yield of FDCA, and Faradaic efficiency of Ni/CP-1.5, Ni/CP-3.0, and Ni/CP-4.5 samples at 1.36 V. (f) FDCA production rate for Ni/CP-1.5, Ni/CP-3.0 and Ni/CP-4.5 at different potentials. (g) Conversion of HMF, yields of FDCA, and Faradaic efficiency obtained by Ni/CP-1.5 for 10 consecutive cycles of HMFOR at 1.36 V. (h) Activity comparison among various representative catalysts reported in the literature for FDCA yield at different reaction potential.

(Fig. 5a-c). It is observed that a substantial fraction of Ni<sup>2+</sup> within Ni/CP-1.5 transitions to Ni<sup>3+</sup> at a low electrode potential of 1.36 V, and the ratio of Ni<sup>3+</sup>/Ni<sup>2+</sup> increases as the potential is further raised to 1.40 and 1.45 V (Fig. 5a). This result also confirms that a significant portion of NiOOH has not been fully reduced to Ni(OH)<sub>2</sub> at open circuit potentials. Notably, the peak position of Ni 2p<sub>3/2</sub> remains unchanged before and after HMF electrolysis, suggesting the absence of a permanent phase like NiO, which differs from some prior studies [58,59]. This discrepancy may partially stem from the different pre-catalyst being used, i.e., nickel oxide versus nickel sulfide. In principle, this behavior is consistent across Ni/CP-3.0 and Ni/CP-4.5. An intriguing difference was that at 1.36 V, the transformation of Ni<sup>2+</sup> to Ni<sup>3+</sup> was less significant on Ni/CP-3.0 and barely visible on Ni/CP-4.5 (Fig. 5b-c), verifying that the phase transformation is sensitive to the particle aggregation structures and that an ordered structure is more conducive to this transformation.

Nevertheless, it must be acknowledged that the ex situ XPS results presented above cannot directly illustrate the dynamic structural evolution of the catalysts under electrochemical operating conditions. In view of this, herein we have endeavored to investigate the dynamic structure of three Ni/CP samples using *in situ* Raman spectroscopy analysis. As revealed in Fig. 5d-f, at relatively low electrode potentials (i.e., < 1.30 V), two characteristic Raman signals of Ni(OH)<sub>2</sub> can be distinguished at 449 and 527 cm<sup>-1</sup> for all three investigated samples. As the electrode potentials increases up to 1.33 V, the signals of Ni(OH)<sub>2</sub> on Ni/CP-1.5 start vanishing, and two new peaks emerge at 474 and

554 cm<sup>-1</sup> (Fig. 5d), corresponding to the e<sub>g</sub> bending vibration and the A<sub>1g</sub> stretching vibration of Ni<sup>3+</sup>-O in NiOOH [21,60-63]. This result directly demonstrates that the phase transformation of Ni(OH)<sub>2</sub> to NiOOH occurs at ~1.33 V on Ni/CP-1.5 with ordered nanoarray structure. In contrast, Ni/CP-3.0 and Ni/CP-4.5 with disordered aggregation structure show the Raman signals of NiOOH only at considerably higher potentials (Fig. 5e-f, Fig. S18). Moreover, the absence of Raman signal for NiO (508 cm<sup>-1</sup>) across different electrode potentials corroborates the XPS findings [64], confirming that no permanent phase such as NiO is generated during electrolysis.

It's worth noting that the above Raman spectra were collected using a single spot-sweep mode, which might result in misleading interpretations due to the inherent inhomogeneity of the materials. Therefore, herein we also conducted *in situ* Raman mapping analyses based on the characteristic signal of NiOOH at 554 cm<sup>-1</sup> (Fig. 5g-i), and the selected areas for collected the Raman signals are shown in Fig. S19. The peak intensity is comparatively weak at 1.30 V for Ni/CP-1.5, indicating an almost negligible presence of NiOOH species (Fig. 5g). But when the potential escalates to 1.33 V, the intensity of this peak significantly expands, signifying the dominance of NiOOH species on the electrode surface. For Ni/CP-3.0 and Ni/CP-4.5 samples, the presence of NiOOH species becomes prominent at potentials of 1.36 and 1.39 V, respectively, as indicated in Fig. 5h-i. Concurrently, the Raman spectra of Ni/CP samples at different time intervals at the same potential reveal that the transformation of Ni(OH)<sub>2</sub> to NiOOH is dependent on potential

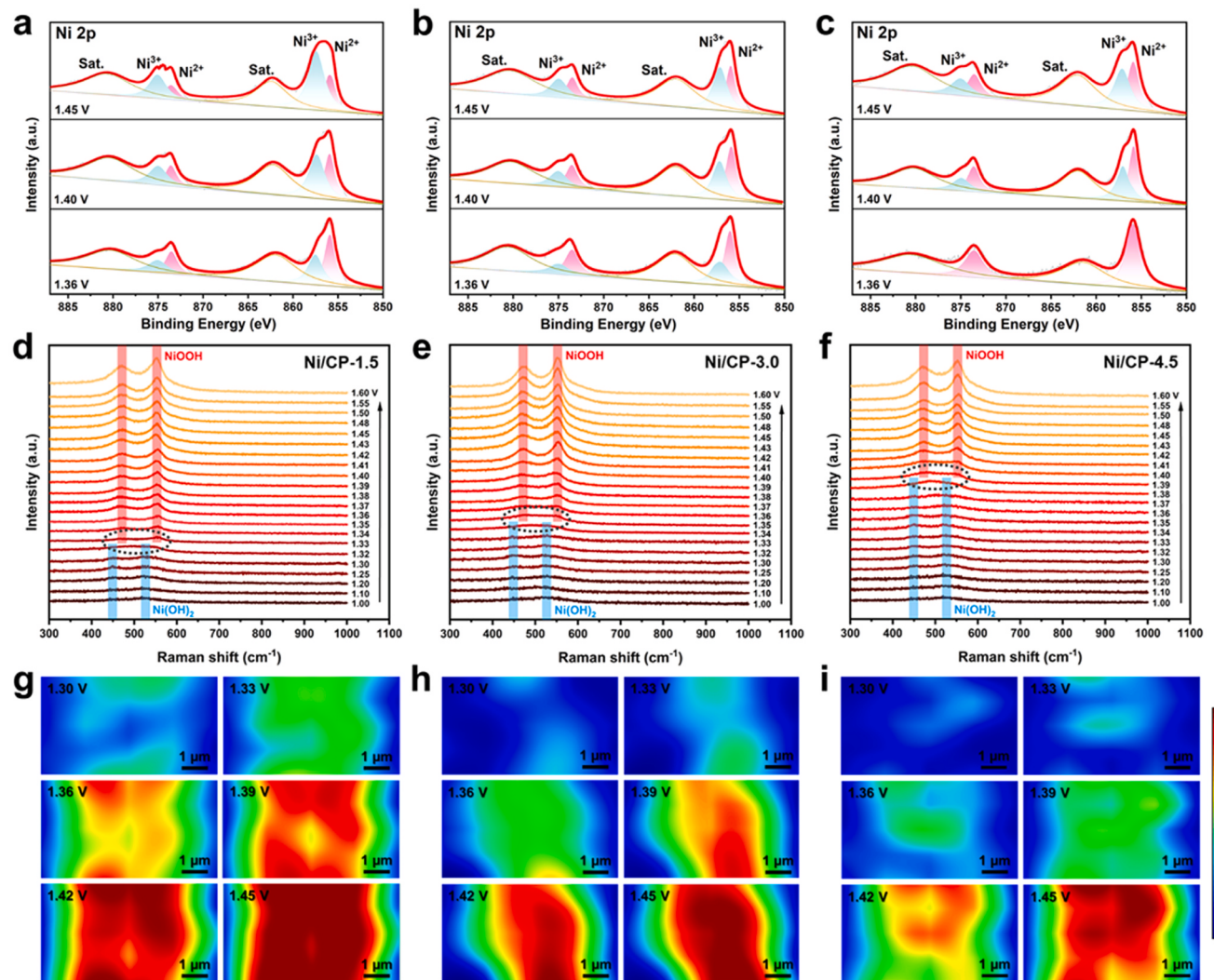
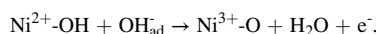


**Fig. 5.** The XPS spectra of (a) Ni/CP-1.5, (b) Ni/CP-3.0, and (c) Ni/CP-4.5 after reacting at different potentials. The in-situ Raman spectra at different potentials for (d) Ni/CP-1.5, (e) Ni/CP-3.0, and (f) Ni/CP-4.5 in 0.1 M KOH. Raman mapping distribution for the main peak of (g) Ni/CP-1.5, (h) Ni/CP-3.0, and (i) Ni/CP-4.5 at 554 cm<sup>-1</sup>.

rather than time (Fig. S20). To elucidate the role of Ni<sup>3+</sup> in the HMFOR, *in situ* Raman analysis was performed on Ni/CP catalysts in 0.1 M KOH electrolyte containing 5 mM HMF. As depicted in Fig. S21, the NiOOH peak at Ni/CP-1.5 is absent until the potential reaches 1.48 V in the presence of HMF, which is significantly more positive than that without HMF. This phenomenon implies that electrically generated NiOOH is spontaneously reduced by HMF during the dehydrogenation processes. When the potential surpasses 1.48 V, the NiOOH signal reappears, indicating that the phase transformation kinetics of Ni<sup>2+</sup> to Ni<sup>3+</sup> is accelerated, and the generated NiOOH has not been fully reduced by the adsorbed HMF.

Based on these findings and prior studies [24,25,65], we propose the following mechanism for HMFOR over Ni/CP catalysts, highlighting the pivotal Ni<sup>2+</sup> to Ni<sup>3+</sup> transition: Initially, as the electrode potential rises, Ni(OH)<sub>2</sub> starts oxidizing to NiOOH through the dehydrogenation reaction:



Subsequently, HMF molecules adsorb on Ni<sup>3+</sup> sites due to the nucleophilic effect [25], followed by HMF oxidation via H transfer to the coordination O atoms, accompanied by the reversion of Ni<sup>3+</sup> to Ni<sup>2+</sup>. It can be seen that the phase transformation of Ni(OH)<sub>2</sub> to NiOOH is thus integral to the HMFOR reaction. The Raman results clearly indicate that

the ordered aggregation structure of particles is conducive to the critical phase transition process, thereby promoting the electrochemical oxidation process of HMF.

The *in situ* electrochemical impedance spectroscopy (EIS) measurements were further undertaken to study the correlation between the phase transformation kinetics and the HMFOR activity. Fig. 6a-c shows the Nyquist plots of Ni/CP samples with different particle aggregation structures in 0.1 M KOH with 5 mM HMF. Firstly, it can be seen that all three samples show nearly vertical lines at low electrode potentials (1.10–1.30 V), indicating a high charge transfer resistance. As the potential increases to 1.35 V, a well-defined semicircle emerges, suggesting a significantly reduced charge transfer resistance due to the occurrence of HMFOR. The other two samples show the same trend, but higher potentials are required for the appearance of the semicircle, which suggest slower reaction kinetics on these two samples, aligning with the previously presented LSV results. Meanwhile, we also fitted the Nyquist plots at different potentials using the equivalent circuit presented in Fig. S8. The quantitative analysis verifies that the Ni/CP-1.5 with ordered nanoarray exhibits the smallest  $R_{\text{ct}}$  (Fig. S22), indicative of the accelerated reaction kinetics for the HMFOR. The corresponding Bode phase plots are displayed in Fig. 6d-f. The high frequency (10<sup>0</sup> – 10<sup>4</sup> Hz) and low frequency (10<sup>-2</sup> – 10<sup>0</sup> Hz) interfaces correspond to surface oxidation (phase transformation) and HMFOR processes,

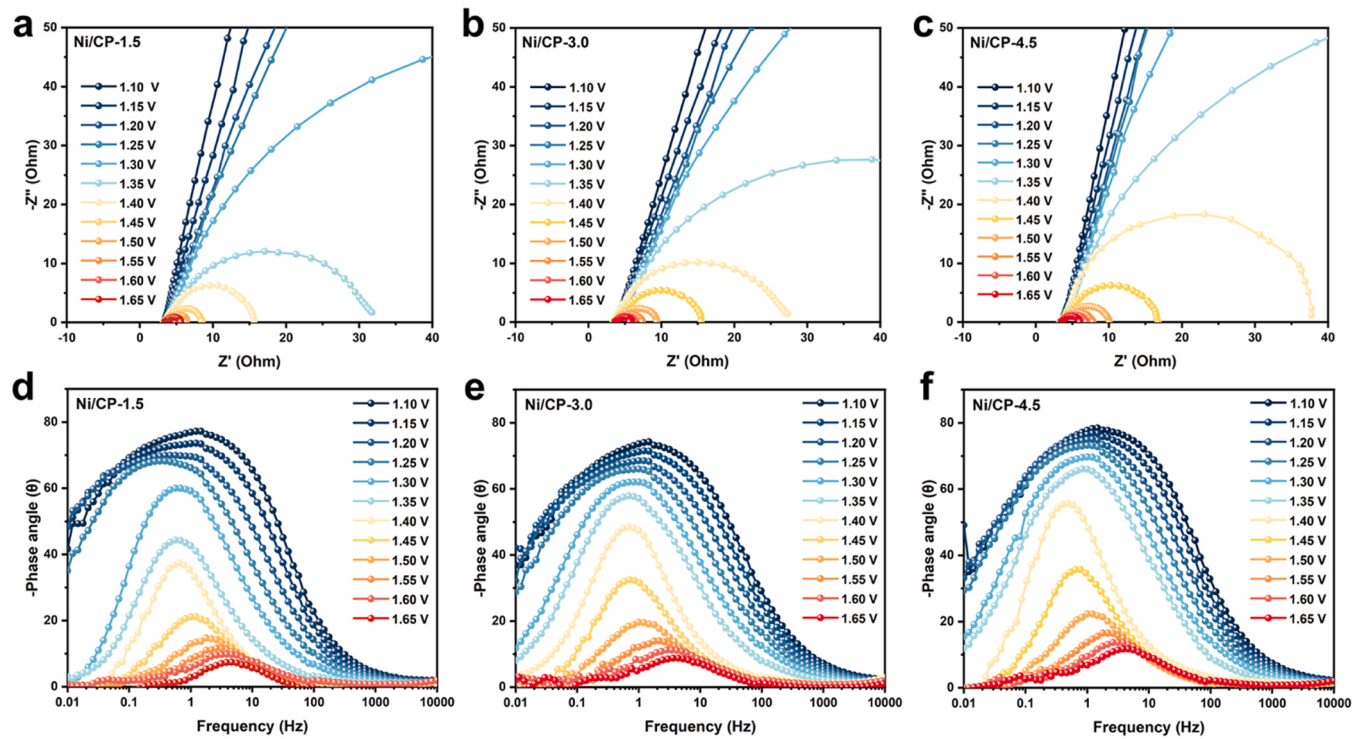


Fig. 6. Nyquist plots and the corresponding Bode plots of Ni/CP-1.5 (a, d), Ni/CP-3.0 (b, e) and Ni/CP-4.5 (c, f) in 0.1 M KOH with 5 mM HMF at varying potentials.

respectively [56,66,67]. Notably, the phase angle peaks within the low frequency range diminish significantly beyond 1.30 V on Ni/CP-1.5, indicating the initiation of the electrochemical HMFOR process. As the potential is elevated to 1.50 V, these peaks shift to the high-frequency domain, indicative of surface oxidation ( $\text{Ni}^{2+}$ - $\text{Ni}^{3+}$ ) on the catalyst. This observation aligns with *in situ* Raman, further suggesting that the initially generated  $\text{Ni}^{3+}$  is promptly reduced back to  $\text{Ni}^{2+}$  by HMF, and the surface oxidation process is not detectable. Similar behavior is also observed on Ni/CP-3.0 and Ni/CP-4.5, but the HMFOR process commences at higher potentials (1.35 V and 1.40 V, respectively). These results clearly demonstrate that the expedited HMFOR kinetics on Ni NPs with ordered nanoarray structure are closely linked to the more facile phase transformation of  $\text{Ni}(\text{OH})_2$ .

Then we are intrigued by the origin of the more facile phase transformation observed in Ni NPs with an ordered structure. Fig. 1 and Fig. 2 show that, fundamentally, all three pristine Ni/CP samples consist of Ni NPs with identical particle size and shape, accompanied by indistinguishable particle crystalline structure and surface electronic structure. The primary difference arising from the particle aggregation structure is their varying interfacial areas between the solid Ni NPs and the aqueous electrolyte, as evidenced by the significantly higher double layer charging capacitance of Ni/CP-1.5 (Fig. 3e). Nevertheless, the impact of the solid-liquid interfacial areas on the phase transformation kinetics of Ni-based electrocatalysts remains mysterious. The phase transformation of  $\text{Ni}(\text{II})$  hydroxide to  $\text{Ni}(\text{III})$  oxyhydroxide corresponds to the oxidative dehydrogenation reaction of  $\text{Ni}(\text{OH})_2$  with hydroxide ions to produce  $\text{NiOOH}$  and water [63,68]. To elucidate this, we compute the energy barriers of this dehydrogenation reaction over the exposed surface and within interlayers of the  $\text{Ni}(\text{OH})_2$  using DFT calculations. It turns out that the dehydrogenation barrier is much lower on the exposed surface (0.41 eV) than that within the interlayers of the nickel double hydroxide (1.54 eV) (Fig. S23), suggesting that the interfacial areas between the catalyst and electrolyte does affect the phase transformation kinetics of Ni-based electrocatalysts. Moreover, the diffusion of water molecules over the exposed surface is also much faster than that within the interlayers (Fig. S24), which may also contribute to the accelerated phase

transformation kinetics.

Based on these results, we can draw a more comprehensive picture about the beneficial role of ordered nanoarray structures toward HMFOR. First, the ordered nanoarray structure can provide a larger electrochemically active surface area, which is essential for maintaining the high FE under high current density conditions. Second, as opposed to the random aggregation of Ni NPs that tend to form a dense structure, the ordered nanoarray structure facilitates the mass transfer of reactive species within the catalyst layer, which is crucial for achieving high current density during the HMFOR. Third, as emphasized in our current study, the ordered nanoarray structure promotes the formation of catalytically active phase, namely  $\text{Ni}(\text{III})$  oxyhydroxide, at a low overpotential, which is considered to play a decisive role in enhancing the overall catalytic efficiency of the Ni NPs. Therefore, the particle aggregation structure affects not only the effective surface area involved in the reaction, but also the dynamic structural evolution of the catalysts, thus offering refreshing approach to developing high performance electrocatalysts. Nevertheless, we have to admit that further extensive studies based on microscopic investigations, especially those under electrochemical operational conditions, as well as theoretical perspectives on electrified surfaces are still needed to deepen our understanding of correlation between the particle aggregation morphology and the dynamic structural evolution of the electrode.

## 5. Conclusion

In summary, we have successfully fabricated Ni NP assemblies with tailored particle aggregation structures, namely ordered nanoarray, disordered nanoarray and random aggregation. It is revealed for the first time that the particle aggregation structure has a profound impact on their HMFOR activity, with the best performance obtained on the ordered nanoarray structure, achieving 99.8 % HMF conversion and 99.2 % FDCA yield at a low potential of 1.36 V. Through comprehensive structural analysis using combined *ex situ* and *in situ* techniques, we have demonstrated that the superior intrinsic activity of the Ni NPs with ordered nanoarray structure can be largely attributed to the reduced

overpotential required for initiating the phase transformation of Ni(II) hydroxide to Ni(III) oxyhydroxide. Furthermore, DFT results suggest that increasing the contact area between catalyst and electrolyte could lower the dehydrogenation barrier of Ni(OH)<sub>2</sub>, thereby promoting the formation of active NiOOH species and accelerating HMFOR. This work clearly demonstrate that the exposed surface area of a catalyst not only influences the number of active sites participating in the reaction, but also impacts the intricate dynamic structural change under operating conditions. Therefore, rationally tailoring interfacial structure of catalyst through particle aggregation structure engineering could be a new toolkit for the design of high-performing electrocatalysts.

### CRediT authorship contribution statement

**Jiansong Wang:** Writing – original draft, Visualization, Validation, Methodology, Investigation, Formal analysis, Data curation, Conceptualization. **Wenru Zhao:** Visualization, Validation, Methodology. **Wei Wang:** Visualization, Software. **Hui Yu:** Formal analysis, Data curation. **Liu-Liu Shen:** Writing – review & editing, Supervision, Methodology, Investigation, Data curation. **Yipu Xu:** Visualization, Resources, Formal analysis. **Donghai Mei:** Writing – review & editing, Supervision, Project administration, Funding acquisition. **Gui-Rong Zhang:** Writing – review & editing, Supervision, Methodology, Funding acquisition, Conceptualization.

### Declaration of Competing Interest

The authors declare that they have no known competing financial interests or personal relationships that could have appeared to influence the work reported in this paper.

### Data availability

Data will be made available on request.

### Acknowledgements

This study is supported by the National Natural Science Foundation of China (No. 22272117) and the National Key R&D Program of China (No. 2023YFB4004704). The authors are thankful to the Analytical & Testing Center of Tiangong University for the technical support in SEM, XRD, TEM, and XPS measurements.

### Appendix A. Supporting information

Supplementary data associated with this article can be found in the online version at [doi:10.1016/j.apcatb.2024.124086](https://doi.org/10.1016/j.apcatb.2024.124086).

### References

- [1] M. Besson, P. Gallezot, C. Pinel, Conversion of biomass into chemicals over metal catalysts, *Chem. Rev.* 114 (2013) 1827–1870.
- [2] I. Scodeller, S. Mansouri, D. Morvan, E. Muller, K.D. Vigier, R. Wischert, F. Jerome, Synthesis of renewable meta-xylylenediamine from biomass-derived furfural, *Angew. Chem. Int. Ed.* 57 (2018) 10510–10514.
- [3] P. Sudarsanam, R. Zhong, S. Van den Bosch, S.M. Coman, V.I. Parvulescu, B.F. Sels, Functionalised heterogeneous catalysts for sustainable biomass valorisation, *Chem. Soc. Rev.* 47 (2018) 8349–8402.
- [4] S. Yang, C. Wu, J. Wang, H. Shen, K. Zhu, X. Zhang, Y. Cao, Q. Zhang, H. Zhang, Metal single-atom and nanoparticle double-active-site relay catalysts: design, preparation, and application to the oxidation of 5-hydroxymethylfurfural, *ACS Catal.* 12 (2022) 971–981.
- [5] Y.X. Lu, T.Y. Liu, C.L. Dong, C.M. Yang, L. Zhou, Y.C. Huang, Y.F. Li, B. Zhou, Y.Q. Zou, S.Y. Wang, Tailoring competitive adsorption sites by oxygen-vacancy on cobalt oxides to enhance the electrooxidation of biomass, *Adv. Mater.* 34 (2022) 2107185.
- [6] Y. Sun, J. Wang, Y. Qi, W. Li, C. Wang, Efficient electrooxidation of 5-hydroxymethylfurfural using Co-doped Ni3S2 catalyst: promising for H2 production under industrial-level current density, *Adv. Sci.* 9 (2022) 2200957.
- [7] H.G. Cha, K.-S. Choi, Combined biomass valorization and hydrogen production in a photoelectrochemical cell, *Nat. Chem.* 7 (2015) 328–333.
- [8] Y.J. Song, Z.H. Li, K. Fan, Z. Ren, W.F. Xie, Y.S. Yang, M.F. Shao, M. Wei, Ultrathin layered double hydroxides nanosheets array towards efficient electrooxidation of 5-hydroxymethylfurfural coupled with hydrogen generation, *Appl. Catal. B Environ.* 299 (2021) 120669.
- [9] M. Park, M. Gu, B.-S. Kim, Tailorable electrocatalytic 5-hydroxymethylfurfural oxidation and H2 production: architecture–performance relationship in bifunctional multilayer electrodes, *ACS Nano* 14 (2020) 6812–6822.
- [10] Z. Xiao, Y.-C. Huang, C.-L. Dong, C. Xie, Z. Liu, S. Du, W. Chen, D. Yan, L. Tao, Z. Shu, G. Zhang, H. Duan, Y. Wang, Y. Zou, R. Chen, S. Wang, Operando identification of the dynamic behavior of oxygen vacancy-rich Co3O4 for oxygen evolution reaction, *J. Am. Chem. Soc.* 142 (2020) 12087–12095.
- [11] G.R. Zhang, L.L. Shen, P. Schmatz, K. Krois, B.J.M. Etzold, Cathodic activated stainless steel mesh as a highly active electrocatalyst for the oxygen evolution reaction with self -healing possibility, *J. Energy Chem.* 49 (2020) 153–160.
- [12] Y.X. Lu, T.Y. Liu, C.L. Dong, Y.C. Huang, Y.F. Li, J. Chen, Y.Q. Zou, S.Y. Wang, Tuning the selective adsorption site of biomass on Co3O4 by Ir single atoms for electrosynthesis, *Adv. Mater.* 33 (2021) 2007056.
- [13] X.-J. Bai, W.-X. He, X.-Y. Lu, Y. Fu, W. Qi, Electrochemical oxidation of 5-hydroxymethylfurfural on ternary metal–organic framework nanoarrays: enhancement from electronic structure modulation, *J. Mater. Chem. A* 9 (2021) 14270–14275.
- [14] W. Chen, C. Xie, Y. Wang, Y. Zou, C.-L. Dong, Y.-C. Huang, Z. Xiao, Z. Wei, S. Du, C. Chen, B. Zhou, J. Ma, S. Wang, Activity origins and design principles of nickel-based catalysts for nucleophilic electrooxidation, *Chem* 6 (2020) 2974–2993.
- [15] Z.Y. He, J.W. Hwang, Z.H. Gong, M.Z. Zhou, N.A. Zhang, X.W. Kang, J.W. Han, Y. Chen, Promoting biomass electrooxidation via modulating proton and oxygen anion deintercalation in hydroxide, *Nat. Commun.* 13 (2022) 3777.
- [16] R. Ge, Y. Wang, Z. Li, M. Xu, S.M. Xu, H. Zhou, K. Ji, F. Chen, J. Zhou, H. Duan, Selective electrooxidation of biomass-derived alcohols to aldehydes in a neutral medium: promoted water dissociation over a nickel-oxide-supported ruthenium single-atom catalyst, *Angew. Chem. Int. Ed.* 61 (2022) e202200211.
- [17] P. Zhou, X.S. Lv, S.S. Tao, J.C. Wu, H.F. Wang, X.X. Wei, T.H. Wang, B. Zhou, Y. X. Lu, T. Frauenheim, X.Z. Fu, S.Y. Wang, Y.Q. Zou, Heterogeneous-interface-enhanced adsorption of organic and hydroxyl for biomass electrooxidation, *Adv. Mater.* 34 (2022) 2204089.
- [18] J. Wu, Z. Kong, Y. Li, Y. Lu, P. Zhou, H. Wang, L. Xu, S. Wang, Y. Zou, Unveiling the adsorption behavior and redox properties of PtNi nanowire for biomass-derived molecules electrooxidation, *ACS Nano* 16 (2022) 21518–21526.
- [19] G.-R. Zhang, S. Wöllner, Hollowed structured PtNi bifunctional electrocatalyst with record low total overpotential for oxygen reduction and oxygen evolution reactions, *Appl. Catal. B Environ.* 222 (2018) 26–34.
- [20] Y. Sun, H. Shin, F. Wang, B. Tian, C.-W. Chiang, S. Liu, X. Li, Y. Wang, L. Tang, W. A. Goddard, M. Ding, Highly selective electrocatalytic oxidation of amines to nitriles assisted by water oxidation on metal-doped  $\alpha$ -Ni(OH)2, *J. Am. Chem. Soc.* 144 (2022) 15185–15192.
- [21] Z.H. Yan, H.M. Sun, X. Chen, H.H. Liu, Y.R. Zhao, H.X. Li, W. Xie, F.Y. Cheng, J. Chen, Anion insertion enhanced electrodeposition of robust metal hydroxide/oxide electrodes for oxygen evolution, *Nat. Commun.* 9 (2018) 2373.
- [22] Z. Qiu, C.-W. Tai, G.A. Niklasson, T. Edvinsson, Direct observation of active catalyst surface phases and the effect of dynamic self-optimization in NiFe-layered double hydroxides for alkaline water splitting, *Energy Environ. Sci.* 12 (2019) 572–581.
- [23] X. Zheng, B. Zhang, P. De Luna, Y. Liang, R. Comin, O. Voznyy, L. Han, F.P. García de Arquer, M. Liu, C.T. Dinh, T. Regier, J.J. Dynes, S. He, H.L. Xin, H. Peng, D. Prendergast, X. Du, E.H. Sargent, Theory-driven design of high-valence metal sites for water oxidation confirmed using *in situ* soft X-ray absorption, *Nat. Chem.* 10 (2017) 149–154.
- [24] L. Lu, C. Wen, H. Wang, Y. Li, J. Wu, C. Wang, Tailoring the electron structure and substrate adsorption energy of Ni hydroxide via Co doping to enhance the electrooxidation of biomass-derived chemicals, *J. Catal.* 424 (2023) 1–8.
- [25] S. Yang, Y. Guo, P. Zhao, H. Jiang, H. Shen, Z. Chen, L. Jiang, X. Xue, Q. Zhang, H. Zhang, Unraveling the electrooxidation mechanism of 5-(Hydroxymethyl)furfural at a molecular level via nickel-based two-dimensional metal–organic frameworks catalysts, *ACS Catal.* 14 (2024) 449–462.
- [26] B. Zhou, Y.Y. Li, Y.Q. Zou, W. Chen, W. Zhou, M.L. Song, Y.J. Wu, Y.X. Lu, J.L. Liu, Y.Y. Wang, S.Y. Wang, Platinum modulates redox properties and 5-hydroxymethylfurfural adsorption kinetics of Ni(OH)2 for biomass upgrading, *Angew. Chem. Int. Ed.* 60 (2021) 22908–22914.
- [27] M. Zubair, P. Kumar, M. Klingenhof, B. Subhash, J.A. Yuwono, S. Cheong, Y. Yao, L. Thomsen, P. Strasser, R.D. Tilley, N.M. Bedford, Vacancy promotion in layered double hydroxide electrocatalysts for improved oxygen evolution reaction performance, *ACS Catal.* 13 (2023) 4799–4810.
- [28] Y.K. Bai, Y. Wu, X.C. Zhou, Y.F. Ye, K.Q. Nie, J.O. Wang, M. Xie, Z.X. Zhang, Z. J. Liu, T. Cheng, C.B. Gao, Promoting nickel oxidation state transitions in single-layer NiFeB hydroxide nanosheets for efficient oxygen evolution, *Nat. Commun.* 13 (2022) 6094.
- [29] J. VandeVondele, M. Krack, F. Mohamed, M. Parrinello, T. Chassaing, J. Hutter, QUICKSTEP: fast and accurate density functional calculations using a mixed gaussian and plane waves approach, *Comput. Phys. Commun.* 167 (2005) 103–128.
- [30] S. Goedecker, M. Teter, J. Hutter, Separable dual-space Gaussian pseudopotentials, *Phys. Rev. B: Condens. Matter* 54 (1996) 1703–1710.
- [31] M. Krack, M. Parrinello, All-electron Ab-initio molecular dynamics, *Phys. Chem. Chem. Phys.* 2 (2000) 2105–2112.
- [32] C. Hartwigsen, S. Goedecker, J. Hutter, Relativistic separable dual-space Gaussian pseudopotentials from H to Rn, *Phys. Rev. B* 58 (1998) 3641–3662.

[33] J. VandeVondele, J. Hutter, Gaussian basis sets for accurate calculations on molecular systems in gas and condensed phases, *J. Chem. Phys.* 127 (2007) 114105.

[34] J.P. Perdew, K. Burke, M. Ernzerhof, Generalized gradient approximation made simple, *Phys. Rev. Lett.* 77 (1996) 3865–3868.

[35] T.T. Zhou, Z. Cao, P. Zhang, H.Y. Ma, Z. Gao, H. Wang, Y. Lu, J. He, Y.F. Zhao, Transition metal ions regulated oxygen evolution reaction performance of Ni-based hydroxides hierarchical nanoarrays, *Sci. Rep.* 7 (2017) 46154.

[36] S. Grimme, J. Antony, S. Ehrlich, H. Krieg, A consistent and accurate Ab initio parametrization of density functional dispersion correction (DFT-D) for the 94 elements H–Pu, *J. Chem. Phys.* 132 (2010) 154104.

[37] G. Henkelman, B.P. Uberuaga, H. Jónsson, A climbing image nudged elastic band method for finding saddle points and minimum energy paths, *J. Chem. Phys.* 113 (2000) 9901–9904.

[38] G.J. Mills, H. Schenter, G. K, Reversible work transition state theory: application to dissociative adsorption of hydrogen, *Surf. Sci.* 324 (1994) 305–337.

[39] Q. Mao, Y. Yu, J. Wang, L. Zheng, Z. Wang, Y. Qiu, Y. Hao, X. Liu, Mitigating the P2–O2 transition and Na+/Vacancy ordering in Na2/3Ni1/3Mn2/3O2 by anion/cation dual-doping for fast and stable Na+ insertion/extraction, *J. Mater. Chem. A* 9 (2021) 10803–10811.

[40] X. Liu, G. Wang, Z. Lv, A. Du, S. Dong, G. Cui, A perspective on uniform plating behavior of Mg metal anode: diffusion limited theory versus nucleation theory, *Adv. Mater.* (2023) 2306395.

[41] A. Pei, G. Zheng, F. Shi, Y. Li, Y. Cui, Nanoscale nucleation and growth of electrodeposited lithium metal, *Nano Lett.* 17 (2017) 1132–1139.

[42] Z. Cai, J. Wang, Z. Lu, R. Zhan, Y. Ou, L. Wang, M. Dahbi, J. Alami, J. Lu, K. Amine, Y. Sun, Ultrafast metal electrodeposition revealed by in situ optical imaging and theoretical modeling towards fast-charging Zn battery chemistry, *Angew. Chem. Int. Ed.* 61 (2022) e202116560.

[43] Y. Li, Q. Wang, L. Zhang, S. Hu, L. Chen, P. He, H. Feng, J. Zhang, H. Ji, X. Ma, K. Li, W. Zhao, Self-assembly of nickel: from nanoparticles to foils with tunable magnetic properties, *CrystEngComm* 21 (2019) 5317–5321.

[44] X. Lu, K.H. Wu, B. Zhang, J. Chen, F. Li, B.J. Su, P. Yan, J.M. Chen, W. Qi, Highly efficient electro-reforming of 5-hydroxymethylfurfural on vertically oriented nickel nanosheet/carbon hybrid catalysts: structure–function relationships, *Angew. Chem. Int. Ed.* 60 (2021) 14528–14535.

[45] F. Wei, M. Luo, J. Lan, F. Xie, L. Cai, T.-S. Chan, M. Peng, Y. Tan, Pd Atomic engineering of nanoporous Ni/NiO for efficient nitrophenol hydrogenation reaction, *ACS Appl. Mater. Inter.* 15 (2023) 26746–26754.

[46] J.T. Ren, L. Chen, W.W. Tian, X.L. Song, Q.H. Kong, H.Y. Wang, Z.Y. Yuan, Rational synthesis of core-shell-structured nickel sulfide-based nanostructures for efficient seawater electrolysis, *Small* 19 (2023) 2300194.

[47] L.L. Chai, A.B. Musa, J.Q. Pan, J.L. Song, Y.Z. Sun, X.G. Liu, In-situ growth of NiAl layered double hydroxides on Ni-based metal-organic framework derived hierarchical carbon as high performance material for Zn-ion batteries, *J. Power Sources* 544 (2022) 231887.

[48] M.W. Louie, A.T. Bell, An investigation of thin-film Ni–Fe oxide catalysts for the electrochemical evolution of oxygen, *J. Am. Chem. Soc.* 135 (2013) 12329–12337.

[49] S. Klaus, Y. Cai, M.W. Louie, L. Trotochaud, A.T. Bell, Effects of Fe electrolyte impurities on Ni(OH)2/NiOOH structure and oxygen evolution activity, *J. Phys. Chem. C* 119 (2015) 7243–7254.

[50] S. Lee, Y.-C. Chu, L. Bai, H.M. Chen, X. Hu, Operando identification of a side-on nickel superoxide intermediate and the mechanism of oxygen evolution on nickel oxyhydroxide, *Chem. Catal.* 3 (2023) 100475.

[51] B.J. Trzesiński, O. Diaz-Morales, D.A. Vermaas, A. Longo, W. Bras, M.T. M. Koper, W.A. Smith, Situ observation of active oxygen species in fe-containing ni-based oxygen evolution catalysts: the effect of pH on Electrochemical Activity, *J. Am. Chem. Soc.* 137 (2015) 15112–15121.

[52] J.F. Xie, X.D. Zhang, H. Zhang, J.J. Zhang, S. Li, R.X. Wang, B.C. Pan, Y. Xie, Intralayered Ostwald Ripening to Ultrathin Nanomesh Catalyst with Robust Oxygen-Evolving Performance, *Adv. Mater.* 29 (2017) 1604765.

[53] Z. Zhao, T. Guo, X. Luo, X. Qin, L. Zheng, L. Yu, Z. Lv, D. Ma, H. Zheng, Bimetallic sites and coordination effects: electronic structure engineering of NiCo-based sulfide for 5-hydroxymethylfurfural electrooxidation, *Catal. Sci. Technol.* 12 (2022) 3817–3825.

[54] B.J. Taitt, D.-H. Nam, K.-S. Choi, A comparative study of nickel, cobalt, and iron oxyhydroxide anodes for the electrochemical oxidation of 5-hydroxymethylfurfural to 2,5-furandicarboxylic acid, *ACS Catal.* 9 (2018) 660–670.

[55] L. Zeng, Y. Chen, M. Sun, Q. Huang, K. Sun, J. Ma, J. Li, H. Tan, M. Li, Y. Pan, Y. Liu, M. Luo, B. Huang, S. Guo, Cooperative Rh-O5/Ni(Fe) Site for Efficient Biomass Upgrading Coupled with H2 Production, *J. Am. Chem. Soc.* 145 (2023) 17577–17587.

[56] S.Q. Li, S.B. Wang, Y.H. Wang, J.H. He, K. Li, Y.J. Xu, M.X. Wang, S.Y. Zhao, X. Ni, L. X. Zhong, J.G. Wang, Doped Mn enhanced NiS electrooxidation performance of HMF into FDCA at industrial-level current density, *Adv. Funct. Mater.* 33 (2023) 2214488.

[57] H. Lei, L. Ma, Q.X. Wan, S.Z. Tan, B. Yang, Z.L. Wang, W.J. Mai, H.J. Fan, Promoting surface reconstruction of NiFe layered double hydroxide for enhanced oxygen evolution, *Adv. Energy Mater.* 12 (2022) 2202522.

[58] J. Zhang, T. Wang, D. Pohl, B. Rellinghaus, R. Dong, S. Liu, X. Zhuang, X. Feng, Interface engineering of MoS2/Ni3S2 heterostructures for highly enhanced electrochemical overall-water-splitting activity, *Angew. Chem. Int. Ed.* 55 (2016) 6702–6707.

[59] S. Yang, Y. Guo, Y. Zhao, L. Zhang, H. Shen, J. Wang, J. Li, C. Wu, W. Wang, Y. Cao, S. Zhuo, Q. Zhang, H. Zhang, Construction of synergistic Ni3S2–MoS2 nanoheterojunctions on Ni foam as bifunctional electrocatalyst for hydrogen evolution integrated with biomass valorization, *Small* 18 (2022) 2201306.

[60] Q.Z. Qian, X.Y. He, Z.Y. Li, Y.X. Chen, Y.F. Feng, M.Y. Cheng, H.K. Zhang, W. T. Wang, C. Xiao, G.Q. Zhang, Y. Xie, Electrochemical biomass upgrading coupled with hydrogen production under industrial-level current density, *Adv. Mater.* 35 (2023) 2300935.

[61] C. Hu, Y. Hu, C. Fan, L. Yang, Y. Zhang, H. Li, W. Xie, Surface-enhanced Raman spectroscopic evidence of key intermediate species and role of NiFe dual-catalytic center in water oxidation, *Angew. Chem. Int. Ed.* 60 (2021) 19774–19778.

[62] Z.Y. Zhou, Y.N. Xie, L.Z. Sun, Z.M. Wang, W.K. Wang, L.Z. Jiang, X. Tao, L.N. Li, X. H. Li, G.H. Zhao, Strain-induced in situ formation of NiOOH species on Co–Co bond for selective electrooxidation of 5-hydroxymethylfurfural and efficient hydrogen production, *Appl. Catal. B Environ.* 305 (2022) 121072.

[63] J. Kang, Y. Xue, J. Yang, Q. Hu, Q. Zhang, L. Gu, A. Selloni, L.-M. Liu, L. Guo, Realizing two-electron transfer in Ni(OH)2 nanosheets for energy storage, *J. Am. Chem. Soc.* 144 (2022) 8969–8976.

[64] Z. Qiu, Y. Ma, T. Edvinsson, Raman investigation of Fe doping influence on catalytic NiO intermediates for enhanced overall water splitting, *Nano Energy* 66 (2019) 104118.

[65] D. Xiao, X. Bao, D. Dai, Y. Gao, S. Si, Z. Wang, Y. Liu, P. Wang, Z. Zheng, H. Cheng, Y. Dai, B. Huang, Boosting the electrochemical 5-hydroxymethylfurfural oxidation by balancing the competitive adsorption of organic and OH- over controllable reconstructed Ni3S2/NiOx, *Adv. Mater.* 35 (2024) 2304133.

[66] D. Chen, Y. Ding, X. Cao, L. Wang, H. Lee, G. Lin, W. Li, G. Ding, L. Sun, Highly efficient biomass upgrading by a Ni–Cu electrocatalyst featuring passivation of water oxidation activity, *Angew. Chem. Int. Ed.* 62 (2023) e202309478.

[67] Y.B. Qi, Y. Zhang, L. Yang, Y.H. Zhao, Y.H. Zhu, H.L. Jiang, C.Z. Li, Insights into the activity of nickel boride/nickel heterostructures for efficient methanol electrooxidation, *Nat. Commun.* 13 (2022) 4602.

[68] J. Kang, G. Liu, Q. Hu, Y. Huang, L.-M. Liu, L. Dong, G. Teobaldi, L. Guo, Parallel nanosheet arrays for industrial oxygen production, *J. Am. Chem. Soc.* 145 (2023) 25143–25149.